Van Der Waals Hybrid Perovskite of High Optical Quality by Chemical Vapor Deposition

*Zhizhong Chen, Yiping Wang, Xin Sun, Yuwei Guo, Yang Hu, Esther Wertz, Xi Wang, Hanwei Gao, Toh-Ming Lu, and Jian Shi**

2D hybrid perovksite $(RNH_3)_2PbX_4$ materials not only serve as ideal platforms to study fundamental physics such as polariton dynamics but also show promise for optoelectronic and electro-optic applications. However, for the preparation of high optical quality crystals, mechanical exfoliation has to be applied in the past. In this work, the vapor phase growth of single crystalline $(C_4H_9NH_3)_2PbI_4$ flakes with high optical quality is reported. Individual single crystalline domains show lateral size about 5–10 µm with defined rectangular shape. Spectroscopic studies show room temperature photoluminescence full width at half maximum of 70 meV and decay lifetime of several nanoseconds, indicating comparably high quality with mechanically exfoliated counterparts. Exciton binding energy 279 ± 46 meV and electron–phonon coupling strength around 20 meV are revealed. This vacuum-based method may provide a solution for integrating layered perovskites into optoelectronic devices and systems.

Organic–inorganic halide hybrid perovskites have emerged as promising optoelectronic materials in recent years with remarkable progress in solar cells, transistors, light emitting diodes, lasers, and photodetectors.[1–4] Generally, the structure of Ruddlesden–Popper phase hybrid perovskites, $(RNH_3)_2(R'NH_3)_{m-1}Pb_mX_{3m+1}$, offers great versatility in their functionalities.[1,5–7] The backbone of hybrid perovskites is formed by the octahedrons of Pb and halide atoms (X), while different alkyl amine groups (RNH_3- or $R'NH_3-$) are inserted among them as spacers. The lead halide octahedrons are separated into different slabs by large alkyl amine ligands (RNH_3-) while smaller ones ($R'NH_3-$, usually methylamonium) distribute within each inorganic slab to sustain the 3D structure. Among different structures, two extreme cases are of special interest: (1) when m goes to infinity, a complete 3D structure is formed due to the absence of larger alkyl amine ligands, e.g., $CH_3NH_3PbI_3$;[4] (2) when m goes to 1, smaller alkyl groups are absent and a complete 2D structure is formed where each single layer of lead halide octahedrons is separated by large alkyl groups, i.e., $(RNH_3)_2PbX_4$.[5] A finite m value which exceeds unity will lead to multilayers of lead halide octahedrons in each individual inorganic slab, e.g., $(C_4H_9NH_3)_2(CH_3NH_3)_3Pb_4I_{13}$.[8]

At present, most of the successful devices are based on 3D perovskites, e.g., $CH_3NH_3PbX_3$, whose long carrier recombination lifetime, long diffusion length, and high carrier mobility make them promising for photovoltaic applications.[3] In comparison, 2D perovskites will not only inherit most of the aforementioned advantages of 3D perovskites but also possess the superiorities of other 2D materials (transitional metal dichalcogenides (TMDCs) and graphene), e.g., high in-plane carrier mobility[9] and easiness in exfoliation or transfer.[10,11] These advantages make them competitive candidates for high-speed transistors, heterostructures, or planar photodetectors. **Figure 1**b showed the polyhedron model of a typical 2D perovskite $(C_4H_9NH_3)_2PbI_4$ where each layer of inorganic octahedrons (drawn grey) is sandwiched between two layers of organic butylamine ligands. As illustrated in Figure 1c, this unique AB stacking of organic–inorganic layers provides a natural quantum well structure where charge carriers are localized within inorganic layers due to the insulating organic ligands. The dielectric confinement and quantum confinement effect both enhance the charge carrier localization such that exciton binding energy amounts to several hundred meV, leading to observable excitonic effect even at room temperature.[10,12–14] In addition, when integrated with 3D perovskites, 2D perovskites serve as protection layers and enhances the moisture stability of the system.[8] These promising properties have attracted intensive investigations into $(RNH_3)_2PbX_4$ with various organic ligands (R− ranging from C_4H_9- to $C_{12}H_{25}-$ and other aromatic compounds)[13,15–17] and halide elements (usually Br and I).[15,17] The great potential of $(RNH_3)_2PbX_4$ is being rapidly revealed, as witnessed by its recent success in solar cells, light-emitting diodes (LEDs), and photodetectors.[8,9,18,19]

Z. Chen, Y. Wang, Y. Guo, Y. Hu, Prof. J. Shi
Department of Materials Science and Engineering
Rensselaer Polytechnic Institute
Troy, NY 12180, USA
E-mail: shij4@rpi.edu

Dr. X. Sun, Prof. E. Wertz, Prof. T.-M. Lu
Department of Physics, Applied Physics and Astronomy
Rensselaer Polytechnic Institute
Troy, NY 12180, USA

X. Wang, Prof. H. Gao
Department of Physics
Florida State University
Tallahassee, FL 32306, USA

DOI: 10.1002/adom.201700373

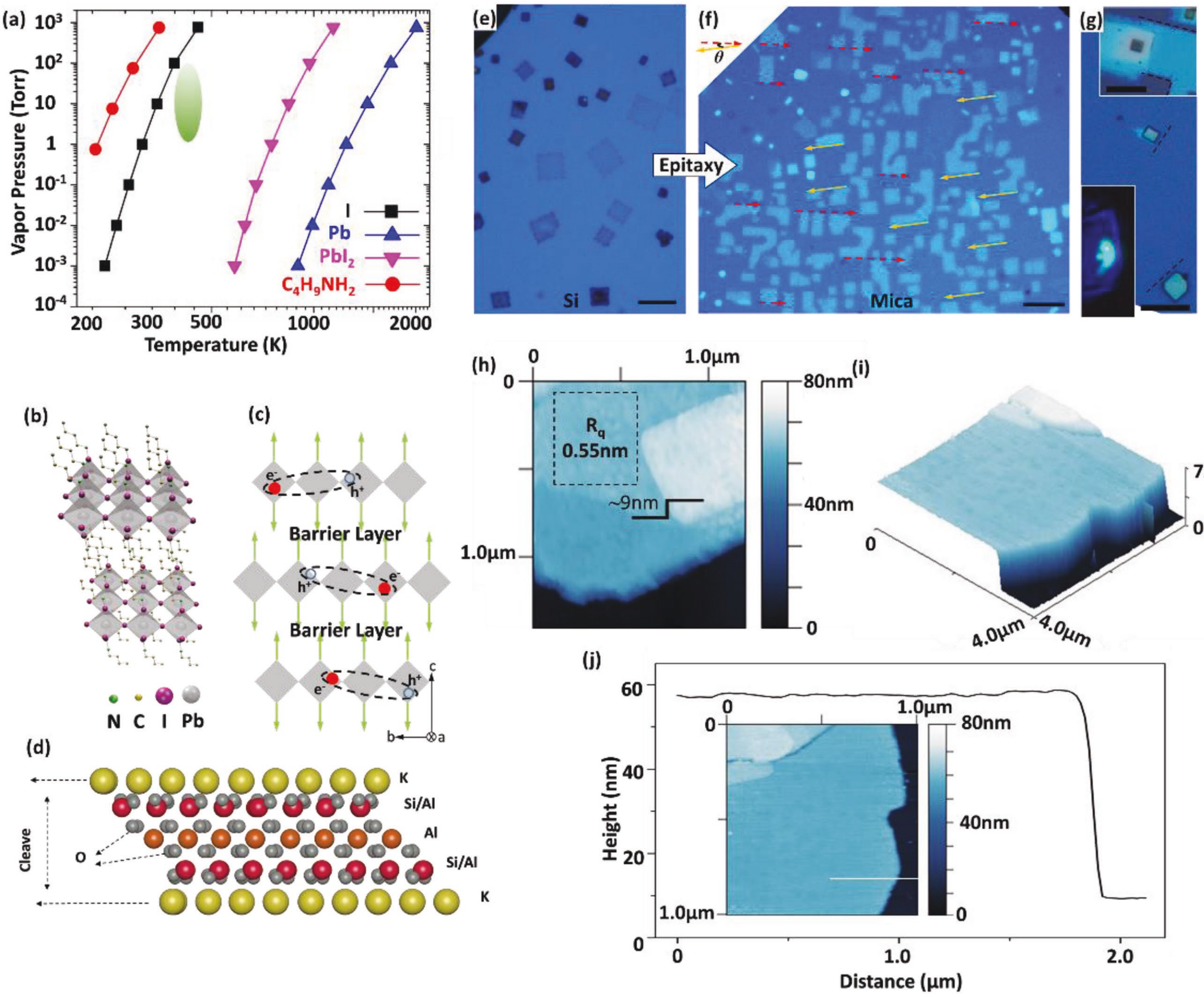

Figure 1. Growth design and results of various $(C_4H_9NH_3)_2PbI_4$ flakes. a) Vapor pressure of reactants at different temperatures. The green circle indicates the chosen heating temperature and chamber pressure range for growth. b) Polyhedron model for $(C_4H_9NH_3)_2PbI_4$ showing the natural quantum well structure. The normal of Pb—I inorganic slabs (*c* axis) was in horizontal direction. Pb—I octahedrons were marked grey, showing the inorganic backbone of the layered perovskite. The butylamine ligands were drawn by chains between inorganic layers as insulating barriers. Hydrogen atoms were omitted. c) *a*-axis projection of the multi quantum well structure where horizontal inorganic Pb—I slabs are drawn as grey squares and organic barrier layers were drawn as vertical green arrows. Excitons were shown in each inorganic layer to demonstrate the spatial confinement effect. d) Layered structure of muscovite mica substrates with cleavage planes horizontally placed. The lack of dangling bonds on potassium-terminated surface enables weak van der Waals interactions with adatoms. e) Nonepitaxial flakes grown on Si by coevaporation. Some flakes showed inhomogeneous thickness. f) Epitaxial flakes grown on mica by coevaporation. The two in-plane orientations were marked by red and orange arrows with an offset θ about 9°. g) Flakes grown on mica in the vicinity of predeposited PbI_2 particles. Main part, the formation of single domain thick flakes on mica, some of which were truncated; lower left inset, bright green photoluminescence from a single domain flake under 405 nm laser excitation; upper right inset, secondary island-like growth atop thin flakes. h) AFM 2D height profile of a thick flake. A newly grown square on top was found, whose height was around 9 nm. The root-mean-square surface roughness (R_q) of the area in dashed box was 0.55 nm, indicating high smoothness. i) 3D height profile of a flake with sharp edge and highly flat surface. j) Height line-scan of another flake shown by inset. The height variation of the plateau part was below 3 nm. The sudden termination at edge was an indication of layered growth behaviors. See main text for more discussions. Scale bars: (g) upper right inset, (e), and (f), 5 µm; (g) main part, 10 µm.

$(RNH_3)_2PbX_4$ films/flakes with different thickness, crystallinity, and coverage can be prepared from various techniques, including solution-phase methods (spin coating[13,16,19,20] or direct evaporation),[5,9] mechanical exfoliation from bulk crystals,[10–12,21] and dual-source vapor deposition.[22] Spin coating is a fast, convenient, and low-cost method that usually gives large-area continuous polycrystalline films. By subsequent solvent vapor annealing, the continuous polycrystalline film could be converted into nanoplates.[19] With precise control of precursor composition and evaporation condition, single-domain $(C_4H_9NH_3)_2PbBr_4$ flakes with one-unit-cell thickness have been prepared by directly evaporating precursor solution.[5] By merit of the weak interlayer bonding, single crystalline flakes with one-unit-cell thickness and low defect density can be directly exfoliated from bulk single crystals, and then transferred onto various substrates. Although these high quality flakes provide great opportunities for studying fundamental properties, the use of solution-phase precursors or the transfer process following exfoliation both hinder the flakes' compatibilities with semiconductor devices or systems where vacuum processing is preferred. In addition to solution-based methods, vacuum approaches have also been attempted. By simultaneously evaporating PbI_2 and organic ammonium iodide RNH_3I at low pressure ($\approx 10^{-6}$ Torr), $(RNH_3)_2PbI_4$ flakes with controllable thickness can be obtained.[22] However, due to the insufficient control over growth process, flakes prepared by dual-source vapor deposition showed high defect density. Apparently, grain boundaries as well as other forms of defects will act as recombination centers and degrade device performance in most occasions, especially for light emitting devices and photodetectors. In addition, noise and artifacts from defects also make fundamental studies rather difficult.[23] Therefore, to fully utilize the desirable properties of $(RNH_3)_2PbX_4$ and further integrate them into optoelectronic devices or systems, single crystalline flakes with low defect density, low surface roughness, and free from transfer or solution-phase precursors are still needed.

Recently, 3D hybrid perovskites $CH_3NH_3PbCl_3$ were grown by vapor phase epitaxy on muscovite mica, a van der Waals substrate whose layered structure was shown in Figure 1d.[24] Due to the weak van der Waals interaction between $CH_3NH_3PbCl_3$ and mica, diffusion of adatoms on substrate was enhanced considerably, consequently single domain large area ultrathin flakes with optically smooth surface were synthesized. In contrast, traditional chemical epitaxy often leads to the formation of islands or clusters and also poses stringent requirements on lattice registration (e.g., III-nitride semiconductors).[25] It is highly likely that van der Waals epitaxy can also be achieved between 2D perovskites and van der Waals substrates.

In this work, we report the vapor phase epitaxy of 2D perovskites $(C_4H_9NH_3)_2PbI_4$. By elaborating growth parameters, individual single crystalline domains with lateral size around 5–10 µm and thickness below 80 nm were obtained, showing epitaxial orientations and optically smooth surface. From temperature dependent photoluminescence studies, the flakes showed nanosecond level carrier decay lifetime and 279 ± 46 meV exciton binding energy, both comparable with mechanically exfoliated counterparts. The role of van der Waals interactions on growth mechanism, flake morphology, and excitonic behaviors was discussed. This vacuum-based method might provide a solution for integrating layered perovskites into optoelectronic devices and systems.

The unique layered structure of 2D perovskites complicates the growth design in vapor phase epitaxy: on the one hand, large organic ligands have very low mobility and it is hard for $(C_4H_9NH_3)_2PbI_4$ molecules to migrate on substrate surface, leading to the formation of clusters rather than flakes;[24] on the other hand, the vapor pressure of PbI_2 is several orders lower in magnitude than that of the organic ligands $C_4H_9NH_2$ due to the higher melting point of the former. As a result, these two components tend to condense in different areas after being carried to the downstream and most of PbI_2 (both Pb atom and I_2 molecules are heavy and immobile) would have been consumed during cooling, with only few left to react with $C_4H_9NH_2 \cdot HI$. To enlarge the overlapping condensation area of PbI_2 and $C_4H_9NH_2 \cdot HI$, and also to reduce the distance between PbI_2 source and deposition zones, the temperature gradient in the downstream area was increased by using a narrow heating belt rather than conventional heaters. Meanwhile, the heating temperature of PbI_2 was reduced slightly to reduce reaction rate. To synthesize thicker flakes, a sufficient supply of PbI_2 must be guaranteed and meantime excessive reaction rate should be avoided. Inspired by the vapor phase growth of high melting point TMDC,[26] PbI_2 powder was spread onto mica surface and the mixture was annealed in the atmosphere of $C_4H_9NH_2 \cdot HI$. In this way, thicker rectangular flakes could be grown in the vicinity of predeposited PbI_2 particles (see Figures S1 and S2 in the Supporting Information). For stability concern, subsequent photoluminescence studies were all based on such thicker flakes.

As expected, single crystalline $(C_4H_9NH_3)_2PbI_4$ flakes were grown on both mica and Si, Figure 1e–g. All domains showed well defined rectangle shape or occasionally truncated by 45°, consistent with the orthorhombic symmetry of $(C_4H_9NH_3)_2PbI_4$. The rectangular shape, which is completely different from hexagon-shaped PbI_2 grown by vapor phase epitaxy (see Figure S2a in the Supporting Information for typical PbI_2 morphology), is one of the indications that the correct perovskite phase has been formed. For thin flakes shown in Figure 1e,f (hereafter such morphologies are referred to as "thin flakes"), the amorphous native SiO_2 layer on Si surface made it impossible for perovskite to orient epitaxially. In contrast, the van der Waals interactions from mica were able to modify the in-plane orientation of perovskite flakes so that two epitaxial directions were observed in Figure 1f, with a slight offset θ around 9°. This offset might be a result of the incompatibility between the sixfold symmetry of mica substrate and the fourfold symmetry of perovskite film (see Figure S5 in the Supporting Information for more structural information). Similar to $CH_3NH_3PbCl_3$,[24] the orientation of $(C_4H_9NH_3)_2PbI_4$ flakes also followed the intrinsic symmetry of perovskite rather than that of mica (pseudohexagonal), consistent to the weak interaction with substrate. By comparing with other results,[5,10,12] we estimated that the thickness of thin films are below 20 nm. By comparing Figure 1e,f, the roughness and thickness of flakes grown on Si were both larger than those on mica, probably due to the amorphous SiO_2 layer which perturbed deposition process. Further characterizations on the morphologies of thin flakes are still needed.

As analyzed before, thicker films were formed in the vicinity of predeposited PbI_2 particles, Figure 1g (hereafter such morphologies are referred to as "thick flakes"). Although equilibrium shape was still maintained, these flakes were too thick to show shiny surface and became yellow, similar to thick PbI_2 epitaxial flakes. Here the 90° epitaxial relation was no longer observable and neighboring domains oriented randomly. This is probably caused by the reduced mobility of perovskite molecules at lower temperature that made in-plane rotation more difficult. Down inset of Figure 1f showed the bright green photoluminescence (PL) from such thick flakes, indicating their stability under laser excitation (to be discussed later). Although a layer-by-layer growth mode is expected in the van der Waals epitaxy of van der Waals materials,[27] certain morphologies like additional small islands or dots were also observed, as shown by the darker squares in the center of Figure 1g upper inset (see Figure S2 in the Supporting Information for more

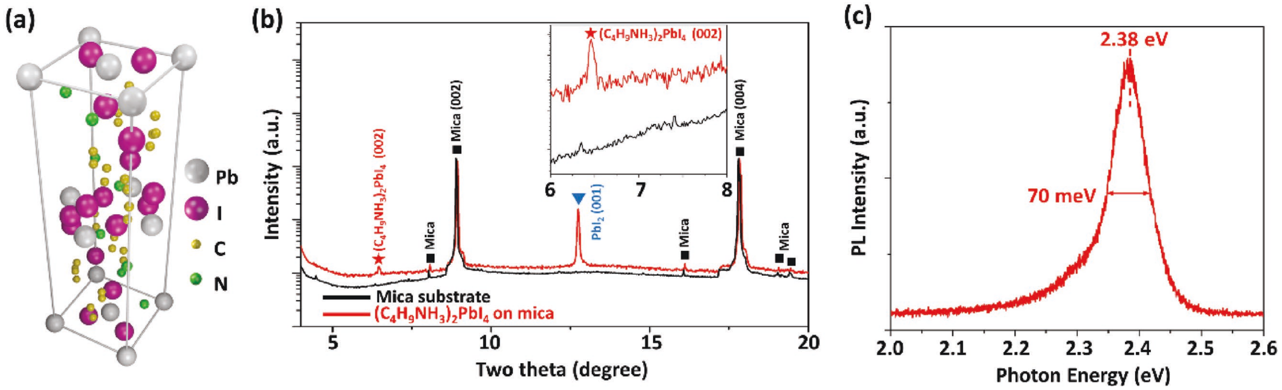

Figure 2. Structural characterization of $(C_4H_9NH_3)_2PbI_4$ flakes. a) A unit cell of $(C_4H_9NH_3)_2PbI_4$ with *c* axis was in vertical direction. Hydrogen atoms were omitted for clarity. b) Log-scale XRD θ–2θ scan of $(C_4H_9NH_3)_2PbI_4$ flakes grown on mica. Residual PbI_2 was detected. The inset showed the magnified perovskite (002) peak compared with bare mica substrate. c) Room temperature steady-state PL spectrum of $(C_4H_9NH_3)_2PbI_4$. The narrow peak at 2.38 eV with FWHM 70 meV corresponded to the emission of $(C_4H_9NH_3)_2PbI_4$. The broad shoulder at lower energy side might be related to photon absorption and re-emission.

images). It should be mentioned that these additional features showed regular rectangular shapes and were completely different from residues of PbI_2 (see Figure S2 in the Supporting Information for more images). Therefore, these indicated new growth/nucleation sites atop crystal surfaces (to be discussed later). Occasionally, flakes in intermediate stage were also formed where equilibrium shape and uniform thickness were not reached yet, as shown in Figure S2 (Supporting Information). As a comparison, when PbI_2 flakes grown from vapor phase were used as PbI_2 source, the same growth setup yielded either randomly oriented single crystalline or compact polycrystalline $(C_4H_9NH_3)_2PbI_4$ flakes, shown in Figure S3 (Supporting Information).

To better understand the surface morphology of flakes as well as the growth behaviors, atomic force microscopy (AFM) was conducted on as-grown thick flakes as Figure 1g. Upper left part of Figure 1g showed a typical 2D height profile. The high surface smoothness observed from optical microscopy can be proved by the low root-mean-square roughness (0.55 nm) measured by AFM in the highlighted region and the low height fluctuation (below 3 nm, corresponding to one unit cell height) shown in the lower part line-scan. The thickness of these flakes ranged between 50 and 80 nm, corresponding to the stacking of around 20–30 unit cells (see next section for more information). Based on the 3D and line-scan height profiles in Figure 1h–j, the flakes terminated sharply and almost vertically at edge. It should be noted that a square flake ≈9 nm thick was detected atop the surface (see Figure S4 in the Supporting Information for more details), showing equilibrium crystal shape. The fact that equilibrium shape can sometimes not be achieved might be the result of the lower mobility of molecules on mica surface compared to that on the crystal surface. Such morphology features as high surface smoothness, surface terrace structure (also shown in Figure S4a,b,d in the Supporting Information) and the sharp terminations were all consistent with layer-by-layer growth mode of layered materials. However, as Figure 1h showed, multiple growth (nucleation) sites were observed in each individual flake, which is rare in the growth of other layered materials like graphene or TMDC where layer-by-layer mode is strictly obeyed. The atypical layer-by-layer growth of $(C_4H_9NH_3)_2PbI_4$ could probably be attributed to the aforementioned low mobility of $(C_4H_9NH_3)_2PbI_4$ molecules. Smaller adatoms (molecules) like carbon show higher mobility on crystal surface and could easily diffuse to growth fronts (edge of kinks) after being adsorbed. As a result, these highly mobile adatoms are not likely to agglomerate as islands, guaranteeing a layer-by-layer growth process in graphene or TMDC. In the case of relatively immobile species, such as $(C_4H_9NH_3)_2PbI_4$ molecules, local agglomerations (islands) are very likely to be formed, leading to multiple growth (nucleation) sites on different layers. Limited migration of adatoms on crystal surfaces often leads to atypical layer-by-layer growth behaviors, e.g., wedding cake growth, in solution-synthesized $(C_4H_9NH_3)_2PbI_4$ nanoplates or vapor-synthesized ZnO nanostructures.[28]

Figure 2a illustrated a unit cell of $(C_4H_9NH_3)_2PbI_4$. Due to slight in-plane distortion, the unit cell followed orthorhombic lattice (space group *Pbca*) where a = 8.86 Å and b = 8.68 Å, while the c spacing is increased to 27.57 Å by organic ligands.[6] The X-ray diffraction (XRD) θ–2θ scan of as-grown flakes was shown in Figure 2b. Due to the small thickness of $(C_4H_9NH_3)_2PbI_4$ flakes, diffraction peaks from mica substrate and residual PbI_2 showed much higher intensity. Nevertheless, by comparison with bare mica substrate, (002) diffraction peak from $(C_4H_9NH_3)_2PbI_4$ was clearly identified, as magnified in the inset. XRD revealed that (001) plane of perovskite grew parallel to (001) of mica and a possible lattice model is proposed in Figure S5 (Supporting Information). A complete set of (002n) peaks could be identified from bulk crystal XRD where (002) showed the highest intensity.[29] In our case, however, the higher order (002n) peaks from $(C_4H_9NH_3)_2PbI_4$ were overwhelmed by the signal from mica or PbI_2. Further characterization as of the in-plane orientation between perovskite flakes and mica are still needed. To further verify the flake composition, room temperature steady-state PL spectrum is shown in Figure 2c. A narrow emission peak at 2.38 eV (522 nm) was observed with full width at half maximum (FWHM) 70 meV. As PL spectrum is a fingerprint for defect states, the single narrow peak around 522 nm could exclude the existence of major defect states in

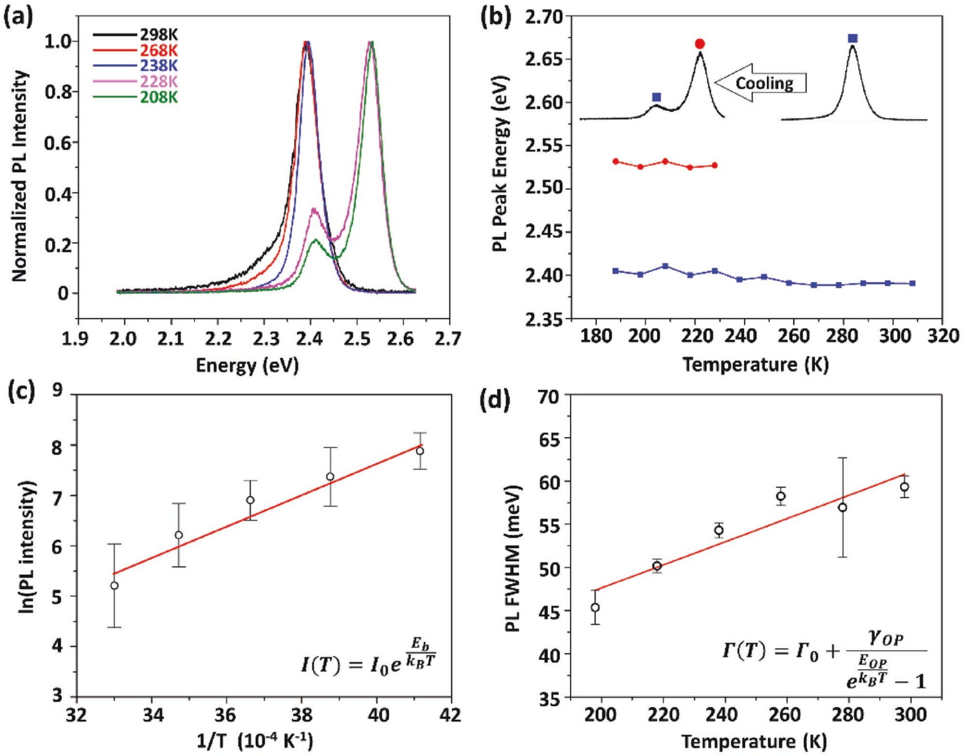

Figure 3. Temperature-dependent PL studies of $(C_4H_9NH_3)_2PbI_4$ flakes. a) Steady-state PL spectra measured from 298 to 208 K. Due to phase transition, a new peak at higher energy side appeared upon cooling while residual signal from high-temperature peak was still observed. b) Temperature dependent PL peak positions upon cooling. The inset demonstrated the transition process from high temperature phase (blue) to low temperature phase (red). Due to kinetic effect, the two phases coexisted in a wide temperature range. c) Arrhenius plot of PL main peak's intensity upon heating from 243 to 303 K. The fitting formula and curve for calculating exciton binding energy were shown inside. d) PL main peak's width upon cooling from 298 to 198 K. The fitting formula and curve for calculating inhomogeneous broadening, optical phonon energy, and coupling strength were shown inside.

the perovskite flakes, indicating comparable crystal quality as mechanically exfoliated counterparts.[12] The PL peak position of PbI_2 was measured to be 2.44 eV (510 nm), thus a redshift of around 60 meV occurred due to the intercalation of insulating organic ligands. This small yet non-negligible transition is another proof that the correct phase was formed. It should be noted that a broad shoulder at lower energy side was observed in addition to the main PL peak (the PL spectrum was fitted by two Gaussian peaks shown in Figure S6 in the Supporting Information). This shoulder was also observed in mechanically exfoliated samples[12] and might be related to photon absorption and re-emission.[30] PL quantum yield and reflection contrast spectrum were also discussed in SI Note 7 and Figure S8 (Supporting Information).

To further understand the excitonic properties of $(C_4H_9NH_3)_2PbI_4$, PL spectra at cryogenic temperatures were analyzed. As shown in **Figure 3**a,b, due to the distortion of organic ligands upon cooling,[31,32] single domain $(C_4H_9NH_3)_2PbI_4$ flakes underwent a phase transition between 238 and 228 K. The low-temperature phase PL peak showed about 125 meV blueshift compared to high-temperature phase. As the phase transition proceeded, the intensity of high temperature peak gradually decreased and the two peaks coexisted over a wide temperature range (see Figure S9 in the Supporting Information for more details). The peak positions from the two phases were compared in Figure 3b. Throughout the whole temperature window, peak energy from high- and low-temperature phases remained around 2.39 and 2.53 eV, respectively, consistent with the results from mechanically exfoliated counterparts.[10] It has been reported in mechanically exfoliated flakes that the domains of high- and low-temperature phases could coexist in one single flake even after cooling to 5 K, this lag in phase transition being attributed to the interaction with substrate.[10] The phase transition temperature was also showed to be affected by flake thickness and strain in solution-processed flakes.[33] Such phenomenon was observed in our case too, Figure S10 (Supporting Information).

The binding energy (E_b) of free excitons is generally approximated as the activation energy of PL emission at higher temperatures where the ionization of excitons becomes the dominant decay mechanism,[17,34] thus the PL emission intensity can be expressed as

$$I(T) = I_0 e^{\frac{E_b}{k_B T}} \tag{1}$$

where $I(T)$ represents the PL intensity at temperature T, E_b represents exciton binding energy and k_B the Boltzmann constant. To calculate E_b, the Arrhenius plot of PL emission intensity at peak energy was shown in Figure 3c. For stability concern, thicker flakes (shown in Figure 1g) were characterized. It should be noted that the temperature window (heating from 243 to 303 K) was chosen such that the perovskite stayed in high-temperature phase and laser damage could be minimized. Upon heating, PL peak intensity decreased and E_b turned out 279 ± 46 meV after Arrhenius fitting. Continuous film prepared by solution method was measured too, showing $E_b \approx 317$ meV, consistent with the values measured in individual flakes, Figure S11 (Supporting Information). E_b of $(C_4H_9NH_3)_2PbI_4$ and similar compounds prepared by cleaving single crystals ranged around 300 meV,[31] comparable with the values measured in this work. E_b of layered hybrid perovskites and ultrathin TMDC is highly sensitive to flake thickness.[10,35] For flakes/films as thick as a few unit cells, a large proportion of the electric lines of force produced by excitons would leak outside of the flake/film. The surrounding dielectric environment (e.g., the substrate beneath or the air/vacuum outside) would adjust the screening between excitons depending on the electric permittivity outside. If the ambient permittivity is smaller than that of the perovskite (like air or vacuum outside), the reduced screening would strengthen the interactions between excitons, leading to larger E_b compared to bulk samples (e.g., thicker than 20 unit cells). For example, E_b of $(C_4H_9NH_3)_2PbI_4$ as thick as a few unit cells increased to 400–500 meV.[10,36] By the same token, E_b will be reduced when the surrounding environment has a larger permittivity (like Si). For bulk samples, as most excitons are screened by the perovskite itself, the impact of dielectric environment becomes negligible. It has been reported that in a defective $(C_6H_5C_2H_4NH_3)_2PbI_4$ film prepared by spin coating, E_b measured by temperature-dependent PL intensity turned out only 60 meV, while the usual value is around 200 meV.[16] The fact that E_b measured in this work is very close to other values measured in bulk indicates the low defect density in our samples.

Electron–phonon coupling in hybrid perovskites have attracted intense research recently.[12,37] It was demonstrated that electron–phonon coupling in $(C_4H_9NH_3)_2PbI_4$ is dominated by homopolar optical phonons through deformation potential, while the contribution from acoustic phonon and longitudinal optical phonons (Fröhlich coupling) are negligible.[12] This is different from 3D hybrid perovskites as well as other polar semiconductors (e.g., GaN) where Fröhlich coupling matters.[38,39] Therefore, after ignoring the contribution from acoustic phonons and impurities, the temperature dependent PL emission line width was fitted according to

$$\Gamma(T) = \Gamma_0 + \frac{\gamma_{OP}}{e^{\frac{E_{OP}}{k_B T}} - 1} \tag{2}$$

where $\Gamma(T)$ stands for the FWHM of PL main peak at temperature T, Γ_0 stands for inhomogeneous broadening which is temperature independent, γ_{OP} and E_{OP} represent the coupling strength and energy of optical phonons, respectively.[12,38] In our calculation, E_{OP} was chosen as 98.8 cm^{-1} (12.28 meV), which represents the out-of-plane stretch mode of I—Pb—I.[12] As shown in Figure 3d, the coupling strength γ_{OP} and Γ_0 turned out to be 19.61 and 28.66 meV, extremely close to the calculated value in mechanically exfoliated samples[12] ($\gamma_{OP} = 20.83$ meV, see SI Note 12 and Figure S12 in the Supporting Information for more details).

Carrier decay lifetime is an important indication of defect density in semiconductors. To further characterize the quality of $(C_4H_9NH_3)_2PbI_4$ flakes, time-resolved PL (TRPL) was carried out on thick flakes. **Figure 4**a–c shows the data from yellow thick flakes shown in Figure 1g main part. At room temperature, only one lifetime component 0.21 ns could be extracted and other component was overwhelmed in background noise. When further cooled down to 238 K, phase transition already occurred in the domain measured and PL emission from both phases were detected simultaneously. The PL decay lifetime at high-temperature phase's emission energy (2.38 eV) increased and a second lifetime component showed up. Such two-component decay profiles were also observed in mechanically exfoliated samples.[12] That decay lifetimes increased after cooling could be explained by the reduced interaction with defects and other recombination channels due to smaller kinetic energy. The short and long lifetime components were both on 1 ns level and could probably be attributed to surface and bulk contributions, respectively, where the former is shorter due to the assistance from surface defects.[23] The PL emission decay at two peak positions and several energy levels in-between (2.38–2.56 eV) were measured and compared in Figure 4b,c. Lifetimes collected from these two phases are similar and showed a monotonic decrease with emission energy increasing. In previous reports, PL from free excitons showed decay lifetime (the longer component) on 1 ns level, while that from bounded excitons was much longer, around 10–30 ns.[17,34]

Decay dynamics in shiny thick flakes shown in Figure 4d–f were similar to yellow thick counterparts. PL emission showed higher intensity and longer lifetime, and two decay lifetimes could be distinguished even at room temperature. By comparing Figure 4b,e, the surface lifetime component turned out similar in both kinds of flakes, while the bulk lifetime of thin flakes (over 3 ns) was about one order in magnitude longer than that of yellow thick flakes, which stays as a puzzle to us.

Single crystalline $(C_4H_9NH_3)_2PbI_4$ flakes were prepared by vapor phase deposition. By elaborating growth setup and reaction rates, individual single crystalline domains with lateral size about 5–10 µm and thickness below 80 nm were obtained, showing certain epitaxial orientations. Thin flakes showed room temperature PL FWHM 70 meV and PL decay lifetime of several nanoseconds, indicating comparable quality and properties as with mechanically exfoliated counterparts. Exciton binding energy around 279 ± 46 meV and optical phonon coupling strength around 20 meV were calculated from temperature dependent PL studies. This vapor phase approach opens up a window on receiving optically high quality 2D perovskite, promising their practical applications in optoelectronics and electro-optics.

Experimental Section

Materials: Lead iodide powder (PbI_2, >99%) and butylamine iodide powder ($C_4H_9NH_2 \cdot HI$, >99%) were purchased from Sigma-Aldrich. Muscovite mica substrates were SPI Grade V-5 with (001) face exposed.

Growth: Thin flakes were grown by coevaporation of PbI_2 and $C_4H_9NH_2 \cdot HI$. Both precursors were loaded into a quartz tube with 1 in. diameter. Then, the quartz tube was loaded into an alumina tube with 1 in. diameter. PbI_2 was placed in zone center heated by a heating belt with center temperature 250–300 °C. $C_4H_9NH_2 \cdot HI$ and as-cleaved mica were placed about 2 in. to the upstream and downstream of PbI_2, respectively. Before heating, the furnace was pumped to base pressure

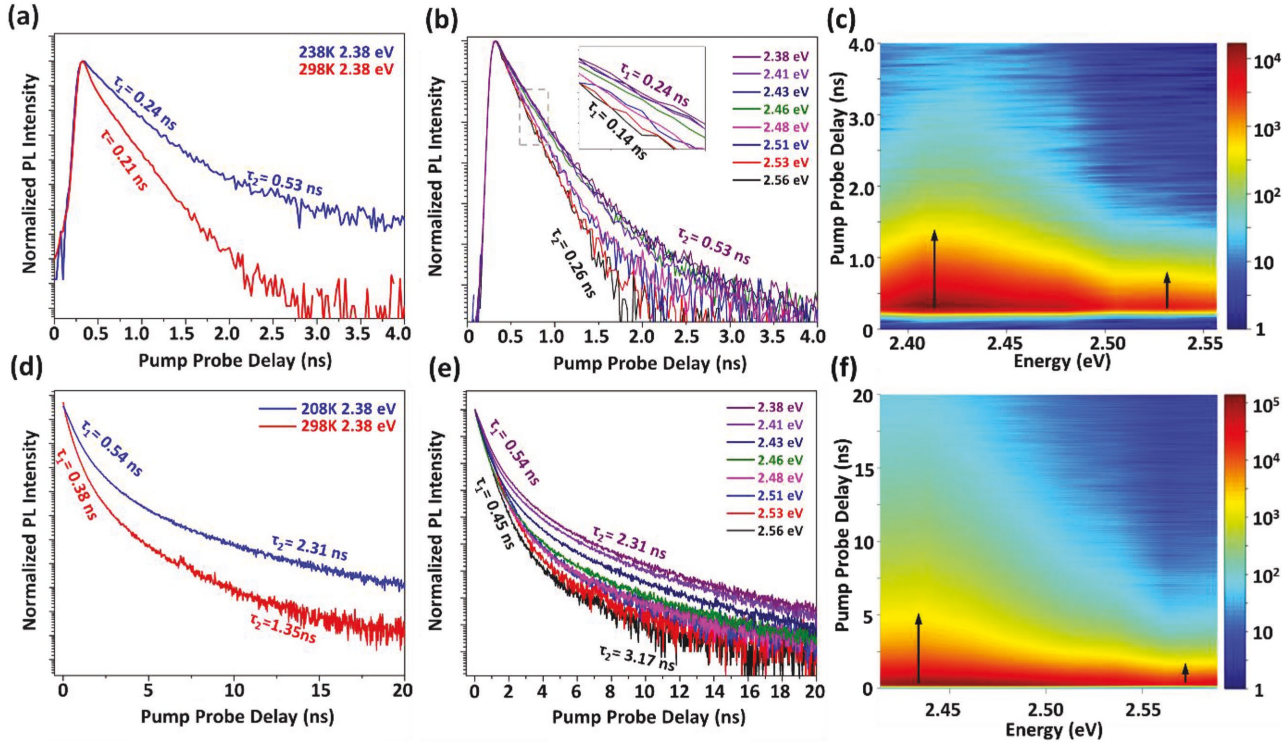

Figure 4. Temperature-dependent PL decay dynamics in $(C_4H_9NH_3)_2PbI_4$ flakes. a–c) Data from yellow thick flakes: (a) PL intensity decay at main peak energy at 298 and 238 K. Lifetime components are indexed inside. (b) PL intensity decay at 238 K collected at different emission energies. The inset magnifies the fast decay component. (c) 2D color contour of log-scale TRPL intensity at 238 K from 0 to 4 ns. The black arrows indicate the emission from high- and low-temperature phases. d–f) Data from shiny thick flakes: (d) PL intensity decay at main peak energy at 298 and 208 K. (e) PL intensity decay at 208 K collected 0–20 ns at different emission energies. f) 2D color contour of log-scale TRPL intensity at 208 K. The black arrows indicate the emission from high- and low-temperature phases.

about 150 mTorr and then high purity Ar was flowed in at 200 sccm until the pressure was stabilized at 70–100 Torr. Then, the furnace was ramped to the heating temperature within 5 min and kept at this temperature for 60–90 min. After heating, the furnace was cooled down naturally to about 100 °C with Ar flowing.

For thick film growth, $C_4H_9NH_2 \cdot HI$ powder was loaded on a quartz boat while PbI_2 powder was spread and then rubbed on the surface of freshly cleaved mica. Both precursors were moved into a quartz tube with 1 in. diameter where $C_4H_9NH_2 \cdot HI$ source was placed about 3 in. to the upstream direction of PbI_2. Then, the quartz tube was loaded into an MTI GSL-1100X tube furnace where $C_4H_9NH_2 \cdot HI$ and PbI_2 source were both placed inside the heating zone (drawn in Figure S1 in the Supporting Information). The tube chamber's wall is made of stainless steel and its diameter is 4 in. Before heating, the furnace was pumped to base pressure about 80 mTorr and then high purity N_2 was flowed in at 200 sccm until the pressure was stabilized at 70–100 Torr. Then, the furnace was ramped to 150 °C within 5 min and kept at this temperature for 30–60 min. During heating, the temperature of PbI_2 powder was about 30 °C lower than $C_4H_9NH_2 \cdot HI$ powder. After heating, the furnace was cooled down naturally to room temperature with N_2 flowing.

Characterizations: Morphology of perovskites was characterized by a Nikon Eclipse Ti-S inverted optical microscope. XRD analyses were done in a Panalytical X'pert PRO MPD system with a Cu source which yields $\lambda\ K_{\alpha 1} = 1.5406$ Å beam. Room-temperature PL characterization was done via a customized PL system consisting of a Picoquant 405 nm pulsed laser, a Nikon Eclipse Ti-S inverted optical microscope, a Princeton Instruments SP-2358 spectrograph, and a Thorlabs 4 Megapixel Monochrome Scientific CCD (charge-coupled device) Camera. Cryogenic PL was carried out by hooking the sample in an INSTEC HCS302 microscope cryostat which can tune the temperature by a MK2000 temperature controller. The cryostat was put under the microscope to get the PL spectrum at each temperature. The surface morphologies of flakes were imaged using an AFM (PSI XE100) in noncontact mode. The AFM tip (HQ: NSC16/Al BS) used has a tip radius of ≈8 nm, a force constant of 45 N m^{-1}, and a resonant frequency of 190 kHz.

For the measurements of exciton binding energy and phonon coupling, three flakes in the same view (under 50× optical microscope) were chosen such that each flake was far enough from its neighboring flakes to minimize light scattering or re-emission. In cryogenic measurement, the sample was loaded into cryogenic stage and cooled down from or heated to room temperature. After reaching the temperature of interest, laser was shone onto each flake for about 0.5 s and the PL signal was collected immediately, then laser was moved away. After collecting the signal of three flakes, the stage was cooled down or heated to the next temperature of interest and the same measurements were repeated. The focused laser spot was about 2 × 2 µm in size with power intensity about 0.02 nJ per pulse. Flakes became more stable to laser illumination at lower temperatures. Due to the short exposure time and low measurement temperatures, all flakes below 10 °C were stable under laser illumination and no damage could be observed from optical microscope.

Supporting Information

Supporting Information is available from the Wiley Online Library or from the author.

Acknowledgements

Y.W., Z.C., and J.S. were supported by the NSF Awards under CMMI 1550941 and CMMI 1635520. E.W. was supported by the NSF Award under CMMI 1635520. H.G. and X.W. acknowledge the financial support from the Energy and Materials Initiative at FSU. The authors appreciate the technical support from Yu Xiang and Prof. Gwo-Ching Wang, the Department of Physics, Applied Physics, and Astronomy, Rensselaer Polytechnic Institute.

Conflict of Interest

The authors declare no conflict of interest.

Keywords

carrier dynamics, chemical vapor deposition, van der Waals perovskites

Received: April 18, 2017
Revised: July 10, 2017
Published online: August 25, 2017

---

[1] B. Saparov, D. B. Mitzi, *Chem. Rev.* **2016**, *116*, 4558.
[2] a) S. A. Veldhuis, P. P. Boix, N. Yantara, M. Li, T. C. Sum, N. Mathews, S. G. Mhaisalkar, *Adv. Mater.* **2016**, *28*, 6804; b) G. Xing, N. Mathews, S. S. Lim, N. Yantara, X. Liu, D. Sabba, M. Grätzel, S. Mhaisalkar, T. C. Sum, *Nat. Mater.* **2014**, *13*, 476; c) H. Zhu, Y. Fu, F. Meng, X. Wu, Z. Gong, Q. Ding, M. V. Gustafsson, M. T. Trinh, S. Jin, X. Y. Zhu, *Nat. Mater.* **2015**, *14*, 636; d) Y. Niu, F. Zhang, Z. Bai, Y. Dong, J. Yang, R. Liu, B. Zou, J. Li, H. Zhong, *Adv. Opt. Mater.* **2015**, *3*, 112; e) S. T. Ha, X. Liu, Q. Zhang, D. Giovanni, T. C. Sum, Q. Xiong, *Adv. Opt. Mater.* **2014**, *2*, 838.
[3] S. D. Stranks, H. J. Snaith, *Nat. Nanotechnol.* **2015**, *10*, 391.
[4] Z.-K. Tan, R. S. Moghaddam, M. L. Lai, P. Docampo, R. Higler, F. Deschler, M. Price, A. Sadhanala, L. M. Pazos, D. Credgington, F. Hanusch, T. Bein, H. J. Snaith, R. H. Friend, *Nat. Nanotechnol.* **2014**, *9*, 687.
[5] L. Dou, A. B. Wong, Y. Yu, M. Lai, N. Kornienko, S. W. Eaton, A. Fu, C. G. Bischak, J. Ma, T. Ding, N. S. Ginsberg, L.-W. Wang, A. P. Alivisatos, P. Yang, *Science* **2015**, *349*, 1518.
[6] D. B. Mitzi, *Chem. Mater.* **1996**, *8*, 791.
[7] D. B. Mitzi, in *Progress in Inorganic Chemistry*, Vol. *48*, K. D. Karlin, Wiley, New York **2007**, p. 1.
[8] H. Tsai, W. Nie, J.-C. Blancon, C. C. Stoumpos, R. Asadpour, B. Harutyunyan, A. J. Neukirch, R. Verduzco, J. J. Crochet, S. Tretiak, L. Pedesseau, J. Even, M. A. Alam, G. Gupta, J. Lou, P. M. Ajayan, M. J. Bedzyk, M. G. Kanatzidis, A. D. Mohite, *Nature* **2016**, *536*, 312.
[9] D. Ma, Y. Fu, L. Dang, J. Zhai, I. A. Guzei, S. Jin, *Nano Res.* **2016**, *10*, 2117.
[10] O. Yaffe, A. Chernikov, Z. M. Norman, Y. Zhong, A. Velauthapillai, A. van der Zande, J. S. Owen, T. F. Heinz, *Phys. Rev. B* **2015**, *92*, 045414.
[11] W. Niu, A. Eiden, G. V. Prakash, J. J. Baumberg, *Appl. Phys. Lett.* **2014**, *104*, 171111.
[12] Z. Guo, X. Wu, T. Zhu, X. Zhu, L. Huang, *ACS Nano* **2016**, *10*, 9992.
[13] a) T. Ishihara, J. Takahashi, T. Goto, *Solid State Commun.* **1989**, *69*, 933; b) N. Kitazawa, M. Aono, Y. Watanabe, *Thin Solid Films* **2010**, *518*, 3199.
[14] N. Kitazawa, T. Ito, D. Sakasegawa, Y. Watanabe, *Thin Solid Films* **2006**, *500*, 133.
[15] I. Teruya, H. Masakatsu, G. Takenari, *Jpn. J. Appl. Phys.* **1995**, *34*, 71.
[16] K. Gauthron, J. S. Lauret, L. Doyennette, G. Lanty, A. Al Choueiry, S. J. Zhang, A. Brehier, L. Largeau, O. Mauguin, J. Bloch, E. Deleporte, *Opt. Express* **2010**, *18*, 5912.
[17] N. Kitazawa, M. Aono, Y. Watanabe, *Mater. Chem. Phys.* **2012**, *134*, 875.
[18] a) Z. Tan, Y. Wu, H. Hong, J. Yin, J. Zhang, L. Lin, M. Wang, X. Sun, L. Sun, Y. Huang, K. Liu, Z. Liu, H. Peng, *J. Am. Chem. Soc.* **2016**, *138*, 16612; b) W. Peng, L. Wang, B. Murali, K.-T. Ho, A. Bera, N. Cho, C.-F. Kang, V. M. Burlakov, J. Pan, L. Sinatra, C. Ma, W. Xu, D. Shi, E. Alarousu, A. Goriely, J.-H. He, O. F. Mohammed, T. Wu, O. M. Bakr, *Adv. Mater.* **2016**, *28*, 3383.
[19] D. Liang, Y. Peng, Y. Fu, M. J. Shearer, J. Zhang, J. Zhai, Y. Zhang, R. J. Hamers, T. L. Andrew, S. Jin, *ACS Nano* **2016**, *10*, 6897.
[20] T. Kenichiro, T. Takayuki, K. Takashi, U. Kenichi, E. Kazuhiro, U. Tsutomu, A. Keisuke, U. Kazuhito, M. Noboru, *Jpn. J. Appl. Phys.* **2005**, *44*, 5923.
[21] X. Wu, M. T. Trinh, D. Niesner, H. Zhu, Z. Norman, J. S. Owen, O. Yaffe, B. J. Kudisch, X. Y. Zhu, *J. Am. Chem. Soc.* **2015**, *137*, 2089.
[22] M. Era, T. Hattori, T. Taira, T. Tsutsui, *Chem. Mater.* **1997**, *9*, 8.
[23] Z. Chen, Y. Wang, Y. Shi, B. Hsu, Z. Yang, J. Shi, *Adv. Electron. Mater.* **2016**, *2*, 1600248.
[24] Y. Wang, Y. Shi, G. Xin, J. Lian, J. Shi, *Cryst. Growth Des.* **2015**, *15*, 4741.
[25] I. Akasaki, *Rev. Mod. Phys.* **2015**, *87*, 1119.
[26] C. Cong, J. Shang, X. Wu, B. Cao, N. Peimyoo, C. Qiu, L. Sun, T. Yu, *Adv. Opt. Mater.* **2014**, *2*, 131.
[27] J. A. Venables, G. D. T. Spiller, M. Hanbucken, *Rep. Prog. Phys.* **1984**, *47*, 399.
[28] a) X. Yin, J. Shi, X. Niu, H. Huang, X. Wang, *Nano Lett.* **2015**, *15*, 7766; b) D. Ma, Y. Fu, L. Dang, J. Zhai, I. A. Guzei, S. Jin, *Nano Res.* **2017**, *10*, 2117.
[29] C. C. Stoumpos, D. H. Cao, D. J. Clark, J. Young, J. M. Rondinelli, J. I. Jang, J. T. Hupp, M. G. Kanatzidis, *Chem. Mater.* **2016**, *28*, 2852.
[30] a) J. Chen, Y. Fu, L. Samad, L. Dang, Y. Zhao, S. Shen, L. Guo, S. Jin, *Nano Lett.* **2017**, *17*, 460; b) Y. Wang, X. Sun, R. Shivanna, Y. Yang, Z. Chen, Y. Guo, G.-C. Wang, E. Wertz, F. Deschler, Z. Cai, H. Zhou, T.-M. Lu, J. Shi, *Nano Lett.* **2016**, *16*, 7974.
[31] T. Ishihara, J. Takahashi, T. Goto, *Phys. Rev. B* **1990**, *42*, 11099.
[32] D. G. Billing, A. Lemmerer, *Acta Crystallogr., Sect. B: Struct. Sci.* **2007**, *63*, 735.
[33] K. Pradeesh, J. J. Baumberg, G. V. Prakash, *Appl. Phys. Lett.* **2009**, *95*, 173305.
[34] N. Kitazawa, Y. Watanabe, *J. Phys. Chem. Solids* **2010**, *71*, 797.
[35] a) A. Chernikov, T. C. Berkelbach, H. M. Hill, A. Rigosi, Y. Li, O. B. Aslan, D. R. Reichman, M. S. Hybertsen, T. F. Heinz, *Phys. Rev. Lett.* **2014**, *113*, 076802; b) D. Wang, B. Wen, Y.-N. Zhu, C.-J. Tong, Z.-K. Tang, L.-M. Liu, *J. Phys. Chem. Lett.* **2017**, *8*, 876.
[36] J.-C. Blancon, H. Tsai, W. Nie, C. C. Stoumpos, L. Pedesseau, C. Katan, M. Kepenekian, C. M. M. Soe, K. Appavoo, M. Y. Sfeir, S. Tretiak, P. M. Ajayan, M. G. Kanatzidis, J. Even, J. J. Crochet, A. D. Mohite, *Science* **2017**, *355*, 1288.
[37] D. B. Straus, S. Hurtado Parra, N. Iotov, J. Gebhardt, A. M. Rappe, J. E. Subotnik, J. M. Kikkawa, C. R. Kagan, *J. Am. Chem. Soc.* **2016**, *138*, 13798.
[38] A. D. Wright, C. Verdi, R. L. Milot, G. E. Eperon, M. A. Pérez-Osorio, H. J. Snaith, F. Giustino, M. B. Johnston, L. M. Herz, *Nat. Commun.* **2016**, *7*, 11755.
[39] S. Rudin, T. L. Reinecke, B. Segall, *Phys. Rev. B* **1990**, *42*, 11218.